

Machine learning spectral indicators of topology

Nina Andrejevic,^{1,2†} Jovana Andrejevic,^{3†} Chris H. Rycroft,^{3,4*} and Mingda Li^{1,5**}

Keywords: machine learning, topological materials, X-ray absorption spectroscopy

Topological materials discovery has emerged as an important frontier in condensed matter physics. Recent theoretical approaches based on symmetry indicators and topological quantum chemistry have been used to identify thousands of candidate topological materials, yet experimental determination of materials topology often poses significant technical challenges. X-ray absorption spectroscopy (XAS) is a widely-used materials characterization technique sensitive to atoms' local symmetry and local chemical environment; thus, it may encode signatures of materials' topology, though indirectly. In this work, we show that XAS can be a potentially powerful tool in identifying materials' topology when it is augmented by machine learning. By labelling computed X-ray absorption near-edge structure (XANES) spectra with their topological class over 16,000 inorganic materials, we establish a machine learning-based classifier of topology with XANES spectral inputs. Our classifier correctly predicts 81% of topological cases and 80% of trivial cases, and for materials containing certain elements, 90% and higher accuracy can be achieved. Given the simplicity of the XAS setup and its compatibility with multimodal sample environments, the proposed machine learning-empowered XAS topological indicator has the potential to discover broader categories of topological materials, such as non-cleavable compounds and amorphous materials. It can also be used to study a variety of field-driven phenomena *in situ*, such as magnetic field-driven topological phase transitions.

Topological materials are defined by the nontrivial topological character of their electronic band structures from which they derive their robust and unconventional properties^{1–5}. The allure of developing these exotic phases into useful applications has garnered widespread efforts to identify and catalogue candidate topological materials to accelerate experimental discovery and synthesis. Recent theoretical progress in topological materials classification based on indicators such as chemistry and crystal symmetry^{6–12} has led to the prediction of over 8,000 topologically non-trivial phases, a vast unexplored territory for experiments. This is strong motivation to develop complementary experimental techniques for high-throughput screening of candidate materials. Current state-of-the-art techniques such as angle-resolved photoemission spectroscopy (ARPES), scanning tunneling microscopy (STM), and quantum transport measurements are commonly used to detect certain topological signatures, but a few limitations remain. Methods that directly probe band topology typically place strict requirements on sample preparation and the sample environment, limiting the range of candidates that can be explored^{13,14}. Other, more indirect methods can be performed over a broader sample space or without significant technical barriers, but the topological character often needs to be in-

ferred with substantial analysis. Neither approach yet fully meets the demands of a high-throughput classification task.

Machine learning methods are increasingly being adapted to enhance processing and analysis of experimental data, particularly in extracting useful information from complex features¹⁵. This presents a potential opportunity to empower high-throughput experimental techniques which may only indirectly probe topological character through machine learning. X-ray absorption spectroscopy (XAS) is widely used to discriminate stoichiometrically similar compounds based on differences in the local chemical environment of their constituent atoms, including their coordination, bond angles, and spatial symmetry. Thus, although indirect, XAS signatures are a potentially useful encoding of topological character which may be deciphered through machine learning methods to diagnose materials topology.

In this work, we have labelled the database of computed X-ray absorption near-edge structure (XANES) spectra¹⁶ according to topological class based on the catalogue of high-quality topological materials predicted by the topological quantum chemistry formalism⁷, and optimized a convolutional neural network architecture to predict the topological class based on XANES spectral inputs. We find that our classifier correctly predicts an overall 81% of topological cases and 80% of trivial cases, and we discuss its comparative success in terms of precision, recall, and F_1 metrics. In particular, for materials containing common elements, including Be, B, Al, Si, Ca, Ti, Zn, Ga, Zr, and Ta, approximately 90% recall for topological materials is achieved overall. Our work suggests the potential of machine learning to uncover topological

¹ Quantum Matter Group, MIT

² Department of Materials Science and Engineering, MIT

³ John A. Paulson School of Engineering and Applied Sciences, Harvard University

⁴ Computational Research Division, Lawrence Berkeley Laboratory

⁵ Department of Nuclear Science and Engineering, MIT

[†] These authors contributed equally to this work.

^{*} Corresponding author: chr@seas.harvard.edu

^{**} Corresponding author: mingda@mit.edu

character embedded in complex spectral features, even though a mechanistic understanding is challenging to acquire.

1 Methods

1.1 Data Assembly

To assemble the training and evaluation datasets, we gathered the entries of 68,347 materials in the Inorganic Crystal Structure Database¹⁷ (ICSD) subject to the high-quality filtering procedure outlined in the topological materials database used for this study⁷. A subset of 7,354 materials in this dataset are classified as topological by the topological quantum chemistry formalism⁷. For the XAS spectra, we used the database of computed K-edge XANES spectra distributed on the Materials Project¹⁶, which are calculated using the Green's function formulation of the multiple scattering theory implemented in FEFF¹⁸. We thus identified all samples with unique entries available on the Materials Project database, obtaining 24,538 examples of which 4,434 were classified as topological, and 20,104 as trivial. Finally, we retained only those samples for which XANES spectra were available for every element of the compound, giving us the final set of 16,458 samples: 3,121 topological, 13,337 trivial. This procedure and the resulting input data structure are illustrated schematically in **Fig. 1(a-b)**. A more detailed summary of data properties is provided in **Table 1**. Additionally, the representation of different elements among topological and trivial examples is shown in **Fig. S1(a-b)**. This fact was considered in evaluating the predictive power of individual elements, which we discuss later. From the assembled dataset of 16,458 samples, training was performed on 70% of the data, reserving 10% for validation and 20% for testing. While samples were randomly distributed among the training, validation, and testing subsets, care was taken to ensure balanced representation of each absorbing element within each subset, as shown in **Fig. S1(c)**. Prior to training, we further augmented the data by shifting each spectrum $\sim \pm 1\text{eV}$ to enforce a tolerance to small perturbations, which simulates experimental conditions, and at the same time increases our data size by a factor of 3.

1.2 Network Architecture Optimization

We posed the task of predicting the topological character as a binary classification problem, identifying each sample as either topological or trivial. We found this to be a sufficient task without necessity to further distinguish between semimetals and insulators, since these are easily differentiated using conventional methods. Computed XANES spectra for each absorbing element in a sample were supplied as input to the machine learning model; a typical set of spectra is shown in **Fig. 1(c)**. Across all samples considered in this work, a total of

Table 1 Number of topological and trivial samples grouped by the number of distinct constituent elements.

Element count	Topological	Trivial
1	29	58
2	761	1,506
3	1,917	6,513
4	380	4,291
5	33	853
6	1	102
7	0	14
Total by class	3,121	13,337
Total overall		16,458

81 different elements were represented, which were regarded as 81 distinct channels in the machine learning model. For each sample, the computed XANES spectra of each absorbing element in the material were re-sampled at 200 evenly-spaced energy values. The complete spectrum for a single sample was stored as a two-dimensional array of 81 columns, with non-zero values in the element channels of that sample's constituent atoms. Each of the 81 element channels was independently standardized prior to inputting into the machine learning algorithm, since the K-edges of different elements are found at very different energy scales. The core network architecture consisted of dimensionality reduction by a sequence of three convolutional and max pooling layers, followed by two fully-connected layers culminating in a single predicted value of topological class, as shown schematically in **Fig. S3(a)**. Convolutional neural networks are a common approach to learning from translationally invariant features such as peaks in a signal; however, they scale easily in the number of model parameters, resulting in a complex model prone to overfitting. Thus, several network design choices were made to constrain the number of model parameters: (1) Convolution kernels learned during training were shared across XANES spectra of all elements, (2) regularization was applied to kernel weights, and (3) dropout was added to the largest fully-connected layer. The number of convolutional layers, regularization strength, dropout rate, kernel size, and hidden layer dimensions were systematically tuned to achieve a network economical in the number of parameters, yet expressive enough to learn clear patterns from considerably diverse data. Additionally, due to the high class imbalance - approximately one topological example for every four trivial examples - as well as an imbalance in representation among different elements, samples were weighted differently to add greater penalty to misclassified topological samples, as well as those containing less represented elements. The network weights were optimized on the training data until no substantial improvement in the validation loss could be observed, as shown in **Fig. S4 (d-e)**. Optimization was performed using the Adam

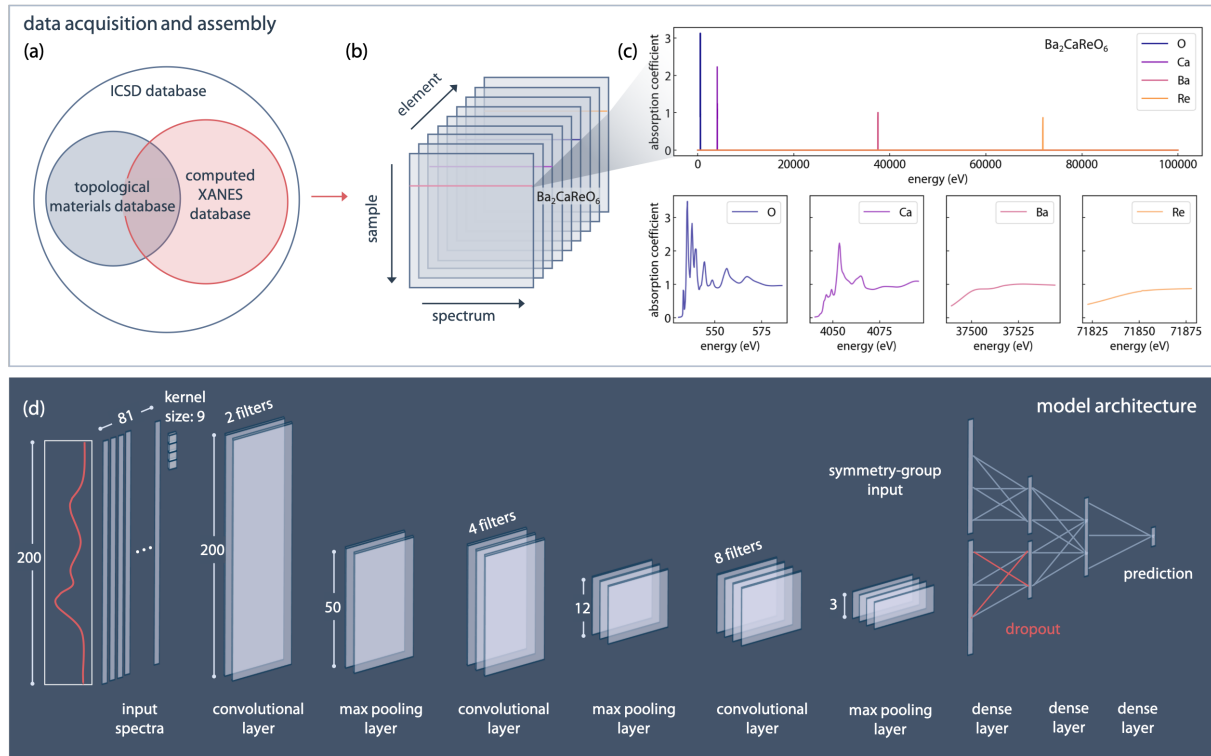


Fig. 1 (a) Candidate samples considered in this study were extracted from the ICSD database according to a high-quality filtering procedure⁷. The subset for which computed XANES spectra were available on the Materials Project database were used in this study, a portion of which are predicted as topological⁷. (b) A total of 81 absorbing elements were represented in the assembled data across 16,458 total samples. The XANES spectrum for each sample was subdivided into 81 distinct energy ranges corresponding to each element's absorption range. (c) A sample complete XANES spectrum (top) with nonzero subsets (bottom) enlarged for clarity. (d) Schematic of the custom neural network architecture with both spectral and symmetry group inputs. A separate pipeline of convolutional and max pooling layers processes XANES spectra, while a fully-connected layer processes symmetry group information. The two outputs are combined to produce the final prediction.

optimizer to minimize the binary cross-entropy loss as is common for binary classification problems. The network was implemented in Python using the TensorFlow and Keras libraries and trained on a Quadro RTX 6000 graphics processing unit (GPU) with 24 GB of random access memory (RAM). All results presented in the main text are evaluations of the test set.

Optimization of this core network architecture led to accurate prediction of approximately 78% of topological and 77% of trivial samples (see **Fig. S3(b)**). About a 3% improvement over this result was achieved by introducing symmetry group as an additional descriptor in the model, motivated by the recent use of symmetry indicators for theoretical prediction of topological materials^{8,10}. This was incorporated in the final network architecture presented in this work and shown schematically in **Fig. 1(d)**. A sample's symmetry group information was encoded as three "one-hot" vectors: The first is a vector of length 7 with a single non-zero indicator of the crystal system, the second a vector of length 32 indicating the point group, and the third a vector of length 230 indicating the space

group. The mixed input of spectral and symmetry group data was accommodated by supplying two separate input channels into initially independent sub-networks; the first sub-network has the core structure described above, while the second accepts the symmetry group encoding, which passes through a single fully-connected dense layer. The outputs of the two separate processing channels are concatenated and passed jointly to a fully-connected layer before entering the final prediction layer with sigmoid activation, which returns a value on (0, 1). We note that the neural network architecture showed mildly better performance over a traditional support vector machine (SVM), which was trained for comparison (see **Fig. S2(b)**).

2 Results

2.1 Exploratory Analysis

Prior to training the neural network classifier, we conducted an exploratory analysis of the assembled XANES spectra to

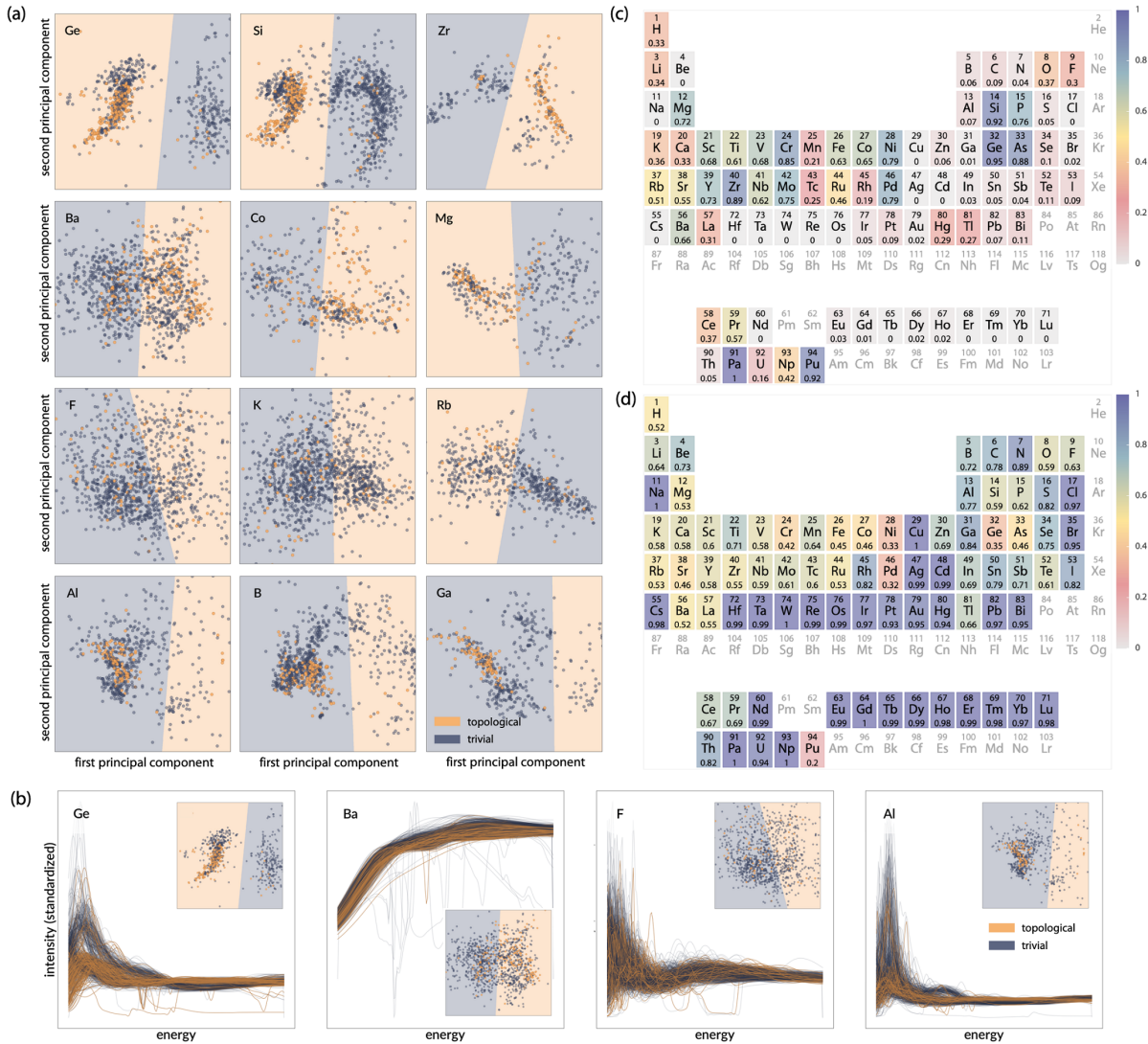


Fig. 2 (a) Decision boundary visualizations of classifications by unsupervised k -means clustering for selected elements along the first two principal components. The clustering performance exhibited four signature patterns: primary segregation of topological examples (first row), balanced segregation of topological and trivial examples (second row), no apparent clustering by class (third row), and clustering not coincident with topological class (fourth row). (b) Representative XANES spectra of selected elements colored by topological class. Inset shows the corresponding decision boundary visualization from (a). (c) Fraction of correctly classified topological examples by element. (d) Fraction of correctly classified trivial examples by element.

gauge the separability by topological class exhibited by different elements. For all examples containing a given element, we performed a principal component analysis (PCA) on the original high-dimensional spectra, and subsequently carried out unsupervised k -means clustering on the first two principal components of the training set. Two clusters were used in order to directly compare the unsupervised classification of the data to the distribution of the known topological class. We visualized the results of the clustering analysis along the

first two principal components for a selection of elements in **Fig. 2(a)**. The decision boundary between the two classes identified by the k -means clustering lies at the intersection of the blue (trivial) and yellow (topological) shaded regions. The examples from all three datasets (training, validation, and testing) are plotted as scattered points in the low-dimensional space and colored according to their known topological class. Additional visualizations are shown in **Fig. S2(a)**. The fraction of scattered points which are clustered consistently with

their topological class is given for each element in **Fig. 2(c)** and **Fig. 2(d)** for topological and trivial examples, respectively. A quick survey of these results reveals a number of elements for which the classification accuracy of topological and trivial examples exhibits a clear trade-off, and a few for which the classification accuracy may be regarded as relatively balanced. We correlated these observations with the decision boundary visualizations and noted four distinct patterns in the result of our unsupervised clustering. For some elements, nearly all topological examples were segregated within a single cluster (first row of **Fig. 2(a)**). This led to a strong score for topological examples but weaker score for trivial ones for elements like Ge, Si, and Zr. Other elements like Ba, Co, and Mg exhibited more balanced classification accuracies between the two topological classes (second row of **Fig. 2(a)**). On the other hand, there were a number of unsuccessful clustering examples, in which the true topological and trivial samples either appeared randomly distributed (third row of **Fig. 2(a)**), or clustering of the data was not coincident with topological class (fourth row of **Fig. 2(a)**). Given that the feature transformations performed in our exploratory analysis were purely linear, its potential to discriminate data between the two classes using certain elements was already encouraging. It further suggested a possible advantage to using more complex, non-linear methods, such as that enabled by a neural network classifier, to improve predictions of both classes.

2.2 Machine Learning Model Performance

We now proceed to a detailed analysis of our highest performing model, the custom neural network architecture with symmetry group input depicted in **Fig. 1(d)**. The strong class imbalance makes simple accuracy a less reliable quantification of model performance; thus, we use three different metrics in assessing the quality of prediction: recall, precision, and F_1 score. Let t_p and t_n denote the number of true positive and true negative predictions, and f_p and f_n denote the number of false positive and false negative predictions, respectively. The metrics are then defined as

$$\text{recall: } r = \frac{t_p}{t_p + f_n} \quad (1a)$$

$$\text{precision: } p = \frac{t_p}{t_p + f_p} \quad (1b)$$

$$F_1 \text{ score: } F_1 = 2 \frac{p \cdot r}{p + r} \quad (1c)$$

These scores may be computed independently for different subsets of the data. We thus provide separate scores for the topological and trivial classes, as presented in **Fig. 3(e)**, as well as a further breakdown for subsets of data containing each absorbing element within the topological class, as shown in **Fig. 3(a-c)**. The recall, which measures the number of correctly identified samples of a given group over all samples

actually belonging to the group, is 81% for the topological and 80% for the trivial class. The trivial class predictions also demonstrate a high precision of 95% or, alternatively, a low false positive rate; few topological samples are mistaken for trivial ones. Conversely, a larger fraction of trivial samples are misclassified as topological, resulting in a relatively low precision (49%) for the topological class. While this result appears less favorable, the high false positive rate for the topological class may in fact be misleading. While we are reasonably confident that true topological samples obtained from the high-quality database are correctly labeled⁷, it is possible that the calculation overlooks some indicators that could render certain topological examples trivial. This suggests that we should prefer to minimize false positives in trivial class predictions, and have less concern for false positives in topological class predictions. The F_1 score, a function of the precision and recall, is valuable as a composite quantifier of prediction quality, but we do bear in mind the effect of precision in the comparatively lower F_1 score of the topological class predictions.

Discussion

We compared the effectiveness of the initial principal component analysis with unsupervised clustering, and that of the final neural network classifier. It is important to acknowledge the differences in approach of the two methods beyond the model complexity. In particular, the PCA was conducted independently for subsets of samples containing a particular element, and the unsupervised clustering results independently suggested that a certain element was either an effective or ineffective predictor of topology based on the clustering accuracy. By contrast, in the neural network classifier, all elements were considered simultaneously, so that a sample's classification was based on information from spectra of all its absorbing elements. This holistic approach does not easily decouple the predictive ability of elements from one another, but we do see some trends maintained across both approaches. A number of lighter transition metals tend to have balanced success in both the PCA and neural network approaches, while the halogens continue to be relatively poor predictors of topology. The elements from the boron and carbon families scored well for both topological and trivial samples in the neural network approach, but not in unsupervised clustering. Interestingly, elements like Be and Ca exhibited some of the highest scores from the neural network classification, which were furthermore equitable among topological and trivial examples (compare **Fig. 3(a)** and **Fig. S4(a)**). This occurred despite the fact that the fraction of topological examples containing either Be or Ca was not necessarily high (see **Fig. S1(c)**), compared to elements like Ce, Ir, and Ni, which had the highest fractional abundance of topological examples, and for which the

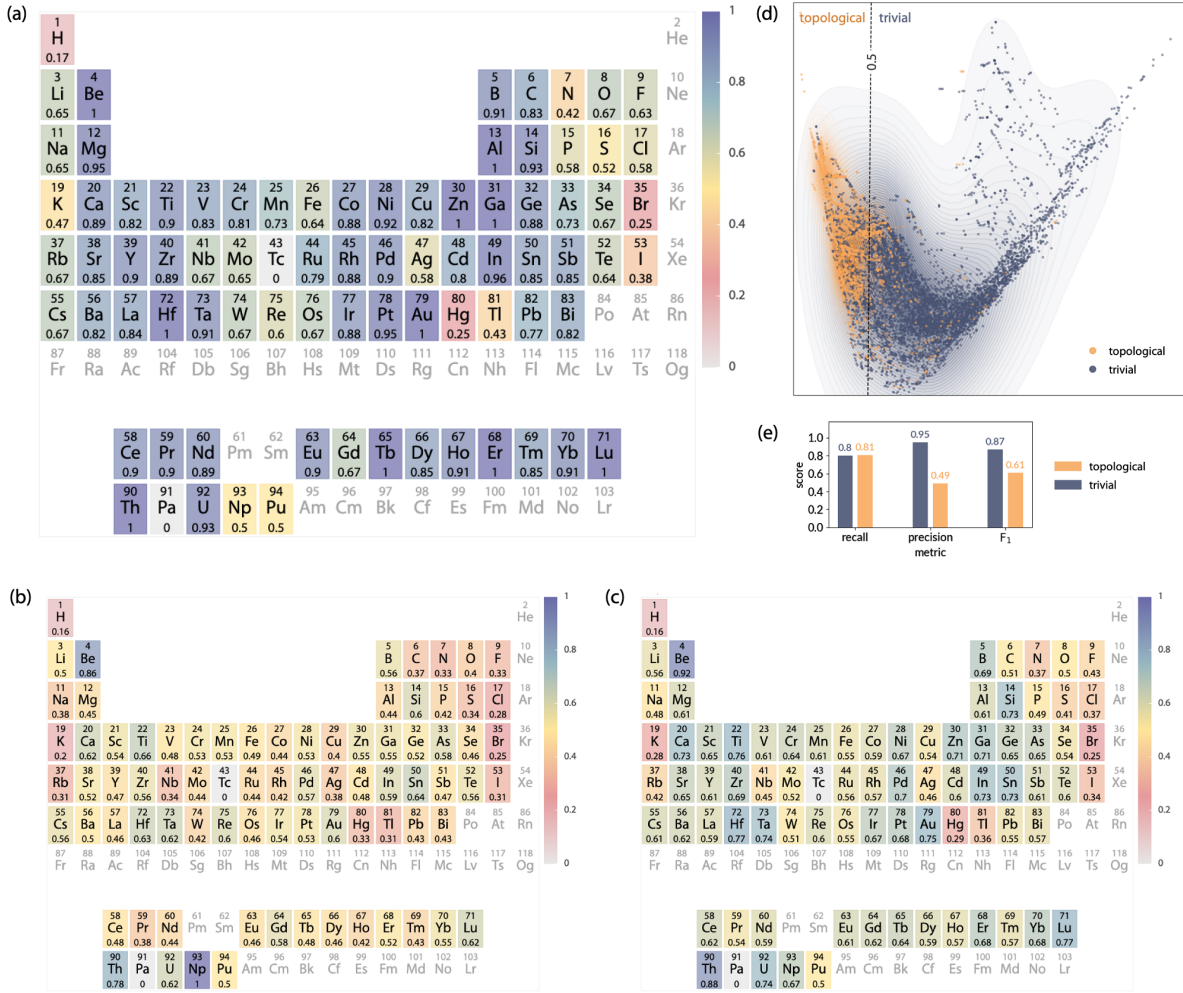


Fig. 3 (a) The recall of the topological class, computed independently for the subsets of test data containing each absorbing element. Each element's entry lists its atomic number, atomic symbol, and recall, and is colored according to the recall. Due to low overall count, topological samples containing Tc and Pa were absent from the testing set; thus their entries are marked as zero. (b) The corresponding precision and (c) F_1 score for each absorbing element's subsamples. (d) Two-dimensional projection of the decision boundary, with the classification threshold set at 0.5. Test data encoded in the low-dimensional space are plotted as scattered points and colored according to true topological class. (e) Overall recall, precision, and F_1 scores for each topology class.

fraction of correctly classified topological examples tended to significantly outweigh that of trivial examples. Moreover, unsupervised clustering was relatively unsuccessful for these two elements, which again may be due to a combination of more complex spectral encoding and more holistic consideration of all absorbing elements present in a given sample by the neural network classifier. We do note that the success of the neural network classifier can be attributed significantly to the presence of particular elements; further work is being pursued to more accurately decouple this contribution from that of more subtle variations in the XAS spectral features for a given ab-

sorber (akin to the PCA approach). Additionally, for certain compounds with sufficient examples, it may be instructive to probe in depth the prediction efficacy of compounds with identical constituent elements but different stoichiometry to highlight the spectral features being addressed by the model.

Conclusion

We explored the predictive power of XAS as a potential discriminant of topological character by training and evaluating a convolutional neural network classifier on more than 16,000

examples of computed XANES spectra¹⁶ labelled according to one of the largest catalogues of topological materials⁷. Our results demonstrate a promising pathway to develop robust experimental protocols for high-throughput screening of candidate topological materials aided by machine learning methods. A number of important extensions are envisioned for this work, such as its application to experimental XANES data, expansion of the energy range to the extended X-ray absorption fine structure (EXAFS) regime, and inquiry into the detailed contribution from spectral features for individual elements. Additionally, the flexibility of the XAS sample environment can further enable the study of materials whose topological phases emerge when driven by electric, magnetic, or strain fields, and even presents the opportunity to study topology with strong disorder and topology in amorphous materials^{19,20}. Thus, machine learning-empowered XAS may be poised to become a simple but powerful experimental tool for topological classification.

Acknowledgments

N.A. acknowledges National Science Foundation GRFP support under Grant No. 1122374. J.A. acknowledges National Science Foundation GRFP support under Grant No. DGE-1745303. N.A. and M.L. acknowledge the support from U.S. Department of Energy (DOE), Office of Science (SC), Basic Energy Sciences (BES), award No. DE-SC0020148.

References

- 1 M. Z. Hasan and C. L. Kane, *Rev. Mod. Phys.*, 2010, **82**, 3045–3067.
- 2 X.-L. Qi and S.-C. Zhang, *Rev. Mod. Phys.*, 2011, **83**, 1057–1110.
- 3 A. Bansil, H. Lin and T. Das, *Rev. Mod. Phys.*, 2016, **88**, 021004.
- 4 N. P. Armitage, E. J. Mele and A. Vishwanath, *Rev. Mod. Phys.*, 2018, **90**, 015001.
- 5 O. Vafek and A. Vishwanath, *Annu. Rev. Condens. Matter Phys.*, 2014, **5**, 83–112.
- 6 B. Bradlyn, L. Elcoro, J. Cano, M. Vergniory, Z. Wang, C. Felser, M. Aroyo and B. A. Bernevig, *Nature*, 2017, **547**, 298–305.
- 7 M. Vergniory, L. Elcoro, C. Felser, N. Regnault, B. A. Bernevig and Z. Wang, *Nature*, 2019, **566**, 480–485.
- 8 F. Tang, H. C. Po, A. Vishwanath and X. Wan, *Nature Physics*, 2019, **15**, 470–476.
- 9 R. Chen, H. C. Po, J. B. Neaton and A. Vishwanath, *Nature Physics*, 2018, **14**, 55–61.
- 10 F. Tang, H. C. Po, A. Vishwanath and X. Wan, *Nature*, 2019, **566**, 486–489.
- 11 T. Zhang, Y. Jiang, Z. Song, H. Huang, Y. He, Z. Fang, H. Weng and C. Fang, *Nature*, 2019, **566**, 475–479.
- 12 K. Choudhary, K. F. Garrity and F. Tavazza, *Scientific reports*, 2019, **9**, 1–8.
- 13 A. Damascelli, Z. Hussain and Z.-X. Shen, *Rev. Mod. Phys.*, 2003, **75**, 473–541.
- 14 S. Suga and A. Sekiyama, *Photoelectron Spectroscopy: Bulk and Surface Electronic Structures*, Springer, 2013, vol. 176.
- 15 G. Carleo, I. Cirac, K. Cranmer, L. Daudet, M. Schuld, N. Tishby, L. Vogt-Maranto and L. Zdeborová, *Rev. Mod. Phys.*, 2019, **91**, 045002.
- 16 K. Mathew, C. Zheng, D. Winston, C. Chen, A. Dozier, J. J. Rehr, S. P. Ong and K. A. Persson, *Scientific data*, 2018, **5**, 180151.
- 17 G. Bergerhoff and I. Brown, *International Union of Crystallography*, 1987.
- 18 J. J. Rehr, J. J. Kas, F. D. Vila, M. P. Prange and K. Jorissen, *Physical Chemistry Chemical Physics*, 2010, **12**, 5503–5513.
- 19 A. Agarwala and V. B. Shenoy, *Phys. Rev. Lett.*, 2017, **118**, 236402.
- 20 E. Prodan, *Journal of Physics A: Mathematical and Theoretical*, 2011, **44**, 113001.

Supplementary Information

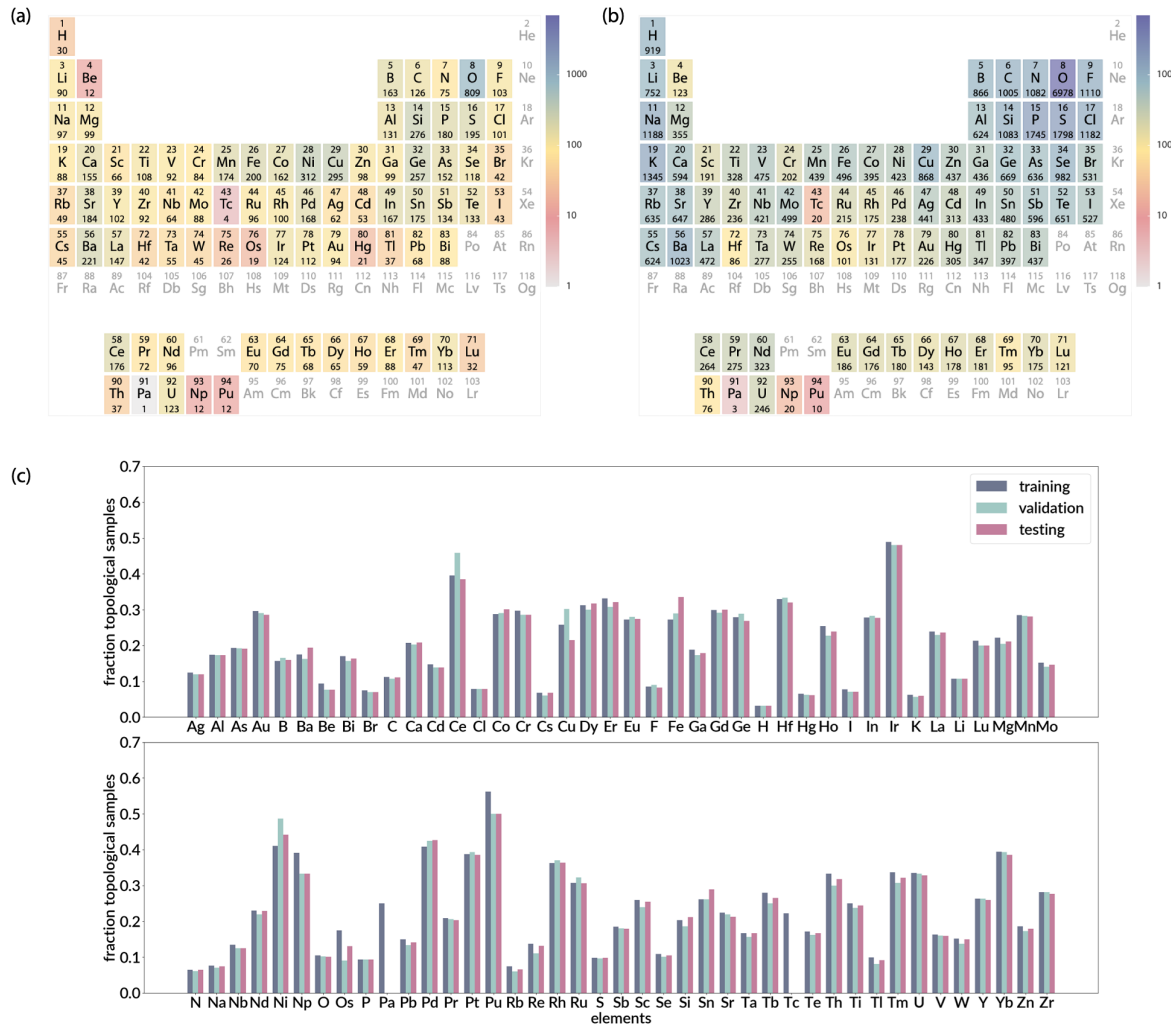


Fig. S1 (a) The total number of topological samples, across training, validation, and testing data, containing each element. Each element's entry includes its atomic number, atomic symbol, and number of samples, and is colored by the number of samples. (b) The total number of trivial samples by element. (c) The fraction of topological samples, by element, in the training, validation, and testing sets. The data split reflects a balanced representation of absorbing elements and topology class across the datasets.

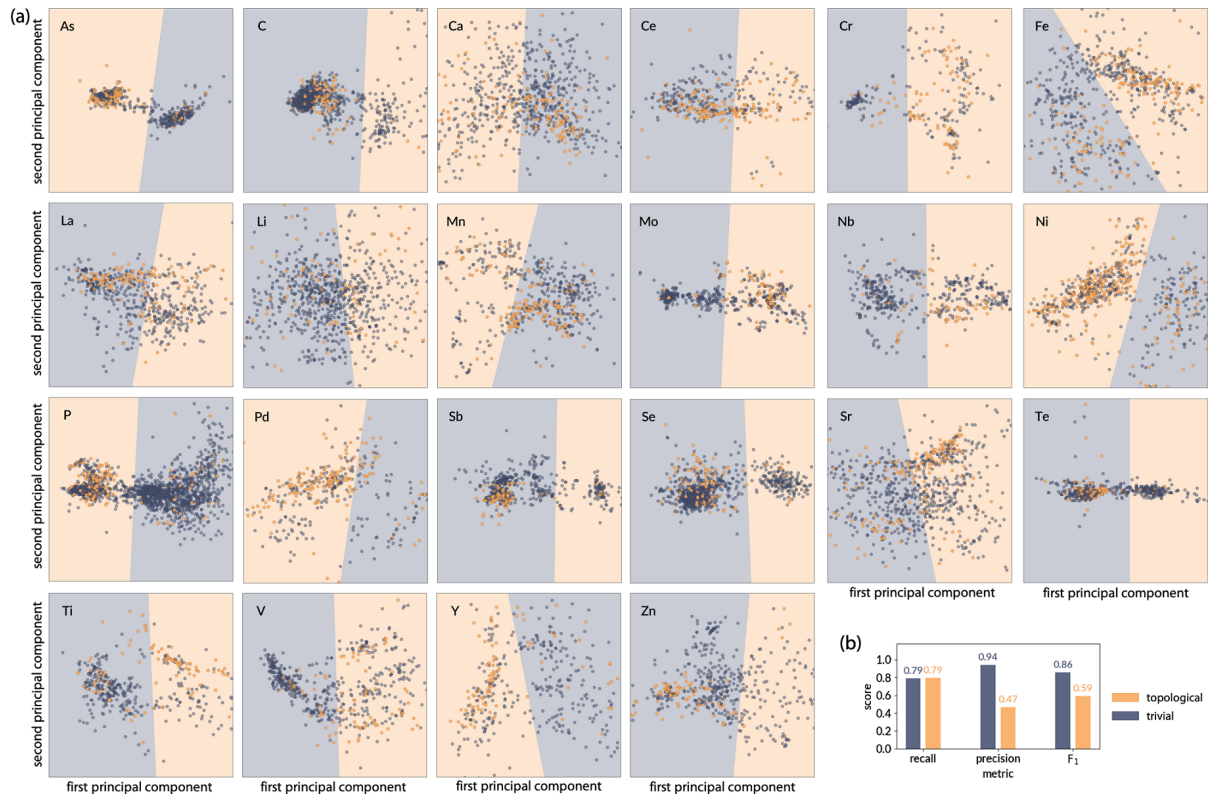


Fig. S2 (a) Additional decision boundary visualizations of classifications by unsupervised k-means clustering for selected elements. (b) Classification performance of a traditional support vector machine according to recall, precision, and F_1 metrics.

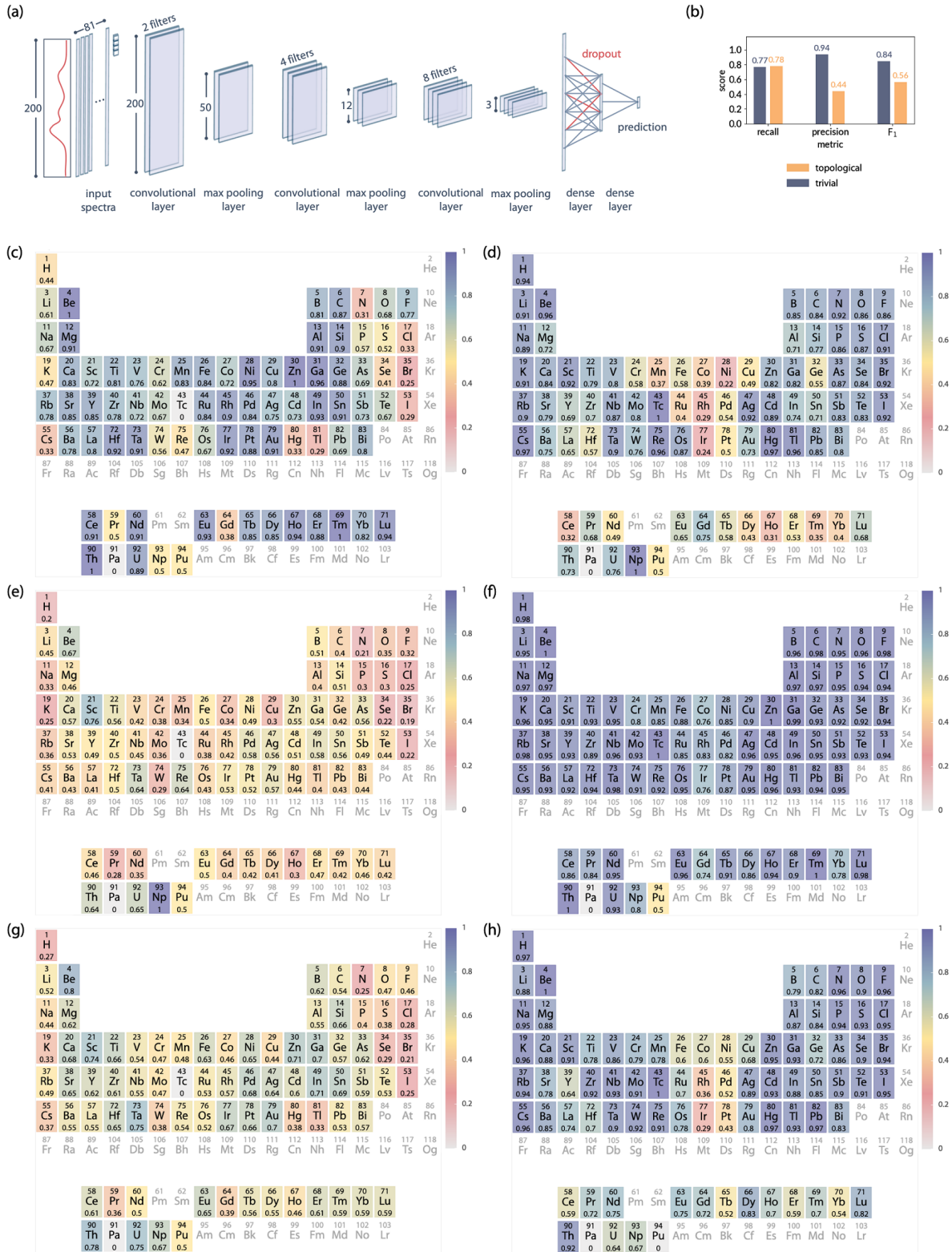


Fig. S3 (a) Schematic of the neural network architecture with only a spectral input (no symmetry group information). (b) Overall recall, precision, and F_1 scores for topological and trivial classes. Element specific recall (c-d), precision (e-f), and F_1 (g-h) scores for topological and trivial examples, respectively.

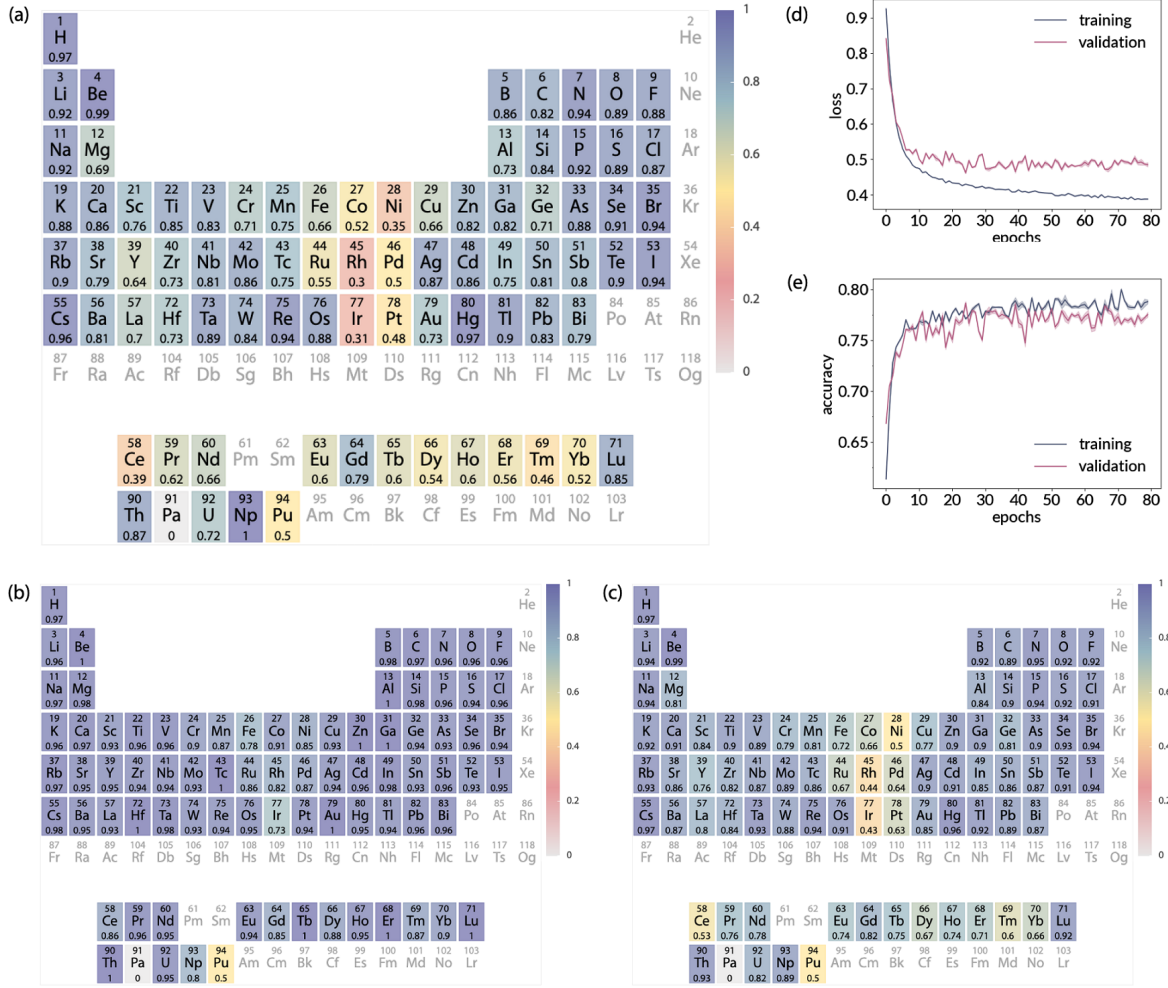


Fig. S4 (a) The recall of the trivial class, computed independently for the subsets of test data containing each absorbing element. Each elements entry lists its atomic number, atomic symbol, and recall, and is colored according to the recall. (b) The corresponding precision and (c) F₁ score for each absorbing elements subsamples. (d) Loss and (e) accuracy of the training and validation sets as a function of epochs used in optimization of the machine learning model.